IEEE Access
Multidisciplinary | Rapid Review | Open Access Journal

Received October 20, 2021, accepted November 5, 2021, date of publication November 8, 2021, date of current version November 16, 2021.

Digital Object Identifier 10.1109/ACCESS.2021.3126738

Intercomparison of Calculated Incident Power Density and Temperature Rise for Exposure From Different Antennas at 10–90 GHz

KUN LI[1,2], (Member, IEEE), YINLIANG DIAO[3], (Member, IEEE), KENSUKE SASAKI[2], (Member, IEEE), ALEXANDER PROKOP[4], (Member, IEEE), DRAGAN POLJAK[5], (Senior Member, IEEE), VICKO DORIC[5], (Member, IEEE), JINGTIAN XI[6], (Member, IEEE), SACHIKO KODERA[7], (Member, IEEE), AKIMASA HIRATA[7], (Fellow, IEEE), AND WALID EL HAJJ[8], (Member, IEEE)

[1]Faculty of Engineering and Design, Kagawa University, Takamatsu 761-0396, Japan
[2]National Institute of Information and Communications Technology, Tokyo 184-8795, Japan
[3]College of Electronic Engineering, South China Agricultural University, Guangzhou 510642, China
[4]Dassault Systèmes SIMULIA, 64293 Darmstadt, Germany
[5]Faculty of Electrical Engineering, Mechanical Engineering and Naval Architecture, University of Split, 21000 Split, Croatia
[6]Foundation for Research on Information Technologies in Society (IT'IS), 8004 Zürich, Switzerland
[7]Department of Electrical and Mechanical Engineering, Nagoya Institute of Technology, Nagoya 466-8555, Japan
[8]Intel Corporation, Wireless RF Laboratory, Intel, 06600 Antibes, France

Corresponding author: Kun Li (li.kun@kagawa-u.ac.jp)

ABSTRACT Recently, international exposure guidelines/standards for human protection from electromagnetic fields were revised. For frequencies between 6-300 GHz, the permissible incident power density is defined as the reference level, which is derived from a new metric ''absorbed/epithelial power density'' based on thermal modeling. However, only a few groups computed the power density and the resultant temperature rise at frequencies greater than 6 GHz, where their exposure conditions were different. This study presents the first intercomparison study of the incident power density and the resultant temperature rise in a human body exposed to different frequency sources ranging from 10 to 90 GHz. This intercomparison aims to clarify the main causes of numerical calculation errors in dosimetry analyses through objective comparison of computation results from six organizations using their numerical methods with various body and antenna models. The intercomparison results indicate that the maximum relative standard deviation (RSD) of peak spatially averaged incident power densities for dipole and dipole array antennas is less than 22.1% and 6.3%, respectively. The maximum RSD of the heating factor, which is defined as the ratio of the peak temperature elevation at the skin surface to the peak spatially averaged incident power density in free space, for dipole and dipole array antennas is less than 43.2% and 41.2%, respectively. The deviations in the heating factors caused by different body models and dielectric/thermal parameters are within 33.1% and 19.6% at 10 and 30 GHz, respectively, when the antenna-to-skin model distance is greater than 5 mm. Under this condition (>5 mm), the deviation in the heating factors caused by different antenna models at 30 GHz does not exceed 26.3%. The fair agreement among the intercomparison results demonstrates that numerical calculation errors of dosimetry analyses caused by the definition of spatially averaged incident power density are marginal.

INDEX TERMS Millimeter wave exposure, radiation safety, standardization, electromagnetic field, dosimetry modeling, skin model, temperature rise, incident power density.

I. INTRODUCTION

Compliance assessment of electromagnetic field (EMF) emitted from wireless devices is one of the essential procedures to protect humans from excessive EMF exposure. Permissible external exposure reference levels or internal basic restrictions have been prescribed in international exposure guidelines and standards, which are established by the International Commission on Non-Ionizing Radiation Protection (ICNIRP) and IEEE International Committee on

The associate editor coordinating the review of this manuscript and approving it for publication was Sandra Costanzo.

This work is licensed under a Creative Commons Attribution 4.0 License. For more information, see https://creativecommons.org/licenses/by/4.0/

Electromagnetic Safety (ICES) Technical Committee (TC) 95. International standards of products for compliance assessment have been established by International Electrotechnical Commission (IEC) TC106 and IEEE ICES TC34 based on the exposure guidelines and standards.

Two international exposure safety guidelines/standards, i.e., ICNIRP guidelines (100 kHz–300 GHz) [1] and IEEE ICES C95.1 standard [2], were revised in 2020 and 2019, respectively. One of the primary changes in the revised guidelines/standards is the introduction of a new exposure metric at frequencies greater than 6 GHz, where the absorbed/epithelial power density [3], [4] was used as the basic restriction (BR) [1] or dosimetric reference limit (DRL) [2]. By contrast, the corresponding incident power density (IPD) in free space is derived using a thermal model (computation) as the reference level (hereafter called reference level (RL) for simplicity) [1] or exposure reference level (ERL) [2] conservatively. Based on the guidelines/standards [1], [2], the IPD should be averaged over an area of 4 cm^2 for frequencies from 6 to 300 GHz. For frequencies higher than 30 GHz, additional criteria of IPD averaged over 1 cm^2 are given with a relaxation of RL/ERL by a factor of 2 for local beam-like exposures [1], [2]. RL and ERL are more practical metrics for evaluating dosimetric quantities than BR/DRL and are easier to conduct compliance assessments. Note that the IPD has been defined as BR in the previous versions of the guidelines/standards [5], [6].

In the exposure guidelines/standards, the definition of the spatial average of IPD is theoretically defined. However, as product safety standards are being developed, one concern is how to define the spatial average of IPD at frequencies greater than 6 GHz while considering practical measurement procedures. The exposure guidelines are intended to prevent excessive temperature rise, so the effect of IPD definition and the averaging method on the temperature rise should also be considered [7]–[18].

With the progress in the development of product standards for compliance assessment, the importance of a more precise and unambiguous definition of the spatial average of IPD based on the correlation of that with temperature elevation became obvious in facilitating practical evaluation procedures. One aspect of this definition is related to the IPD quantity averaged over the prescribed surface area, which can be calculated using two methods:

- Only the components of IPD vectors normal to the averaging surface of the body are used for spatial averaging.
- The magnitudes (norms) of IPD vectors are averaged over the area, irrespective of the orientation.

A working group 5 under Subcommittee 6 of IEEE ICES TC95 has been established to clarify these aspects. Some recent studies have investigated these two IPD definitions by [19]–[26], including oblique incidence for near-field [27], [28] and plane-wave exposure conditions [29]–[32]. However, in this emerging frequency range, a limited number of groups computed the power density and temperature rise in the human body models for EMF exposure above 6 GHz. The cause of numerical computation errors has not been objectively investigated by comparing different numerical methods and models. Such an intercomparison has been conducted for standardization, even in frequency bands of a few GHz [33]. Thus, the first mission of the working group was to perform an intercomparison of the IPD and the resultant temperature rise for dosimetry analysis at frequencies greater than 6 GHz.

This study computed the spatially averaged IPD and the peak temperature rise at the skin surface from 10 to 90 GHz using computational approaches. An intercomparison of numerical calculation errors from six research groups using their simulation codes and commercial EM solvers with various body and antenna models was performed.

TABLE 1. Exposure scenarios.

Antenna type	Frequency [GHz]	Distance [mm]	Organizations
Dipole	10, 30, 60, 90	2, 5, 10, 50, 150	NICT, NITech, SCAU, 3DS, Unisplit, IT'IS
Dipole Array	10, 30, 60, 90	2, 5, 10, 50,150	NICT, NITech, SCAU
Patch Array	30	2, 5, 10	NICT, SCAU, 3DS
Slot Array	30	2, 5, 10	IT'IS, 3DS

II. ANALYTICAL MODEL AND METHOD

A. EXPOSURE SCENARIOS

Six different organizations collaborated to conduct this study: the National Institute of Information and Communications Technology (NICT), Nagoya Institute of Technology (NITech), South China Agricultural University (SCAU), Dassault Systèmes SIMULIA (3DS), Foundation for Research on Information Technologies in Society (IT'IS), and University of Split (UniSplit). Table 1 presents an overview of scenarios evaluated numerically by the participating organizations. The antenna models for numerical simulations, the simplified human body models, and the thermal parameters are described in Sections II-B, II-C, and II-D, respectively.

As presented in Table 1, a separation distance between the antenna and the skin surface ranging from 2 to 150 mm was considered. The ICNIRP guidelines [1] state, "*As a rough guide, distances* $> 2D^2/\lambda$ *[m], between* $\lambda/2\pi$ *and* $2D^2/\lambda$ *[m], and* $< \lambda/2\pi$ *[m] from an antenna correspond approximately to the far-field, radiative near-field and reactive near-field, respectively, where D and* λ *refer to the longest dimension of the antenna and wavelength, respectively, in meters.*" Therefore, some exposure scenarios considered in this study may not be in the applicable range in IPD specified in the safety guidelines [1]. Nonetheless, results for all conditions will be presented in this study because our main purpose is

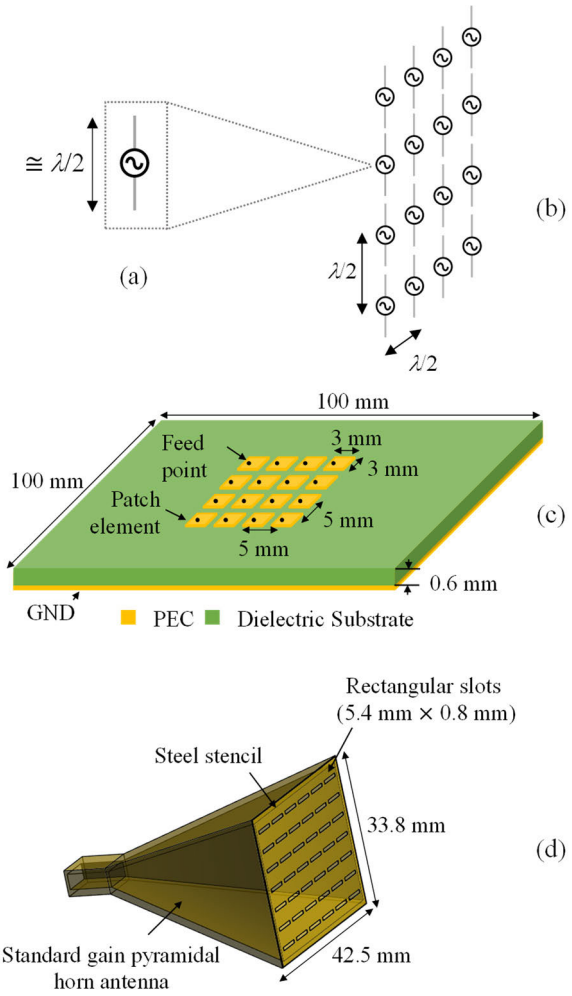

FIGURE 1. Computational antenna models: (a) half-wavelength dipole, (b) a 4 × 4 dipole array, (c) a 4 × 4 patch array at 30 GHz, and (d) a pyramidal horn with a slot array at 30 GHz.

to clarify the computational difference computed by different groups. The thickness of the chassis would be close to 2 mm, so the minimum distance was considered an extreme case. Note that in most wireless device use scenarios, the antenna is not located close to the body to such a separation distance.

B. COMPUTATIONAL ANTENNA MODELS

The antenna models for numerical simulations used by different organizations are illustrated in Fig. 1. The following antenna models were suggested in the discussion of a working group 5 under Subcommittee 6 of IEEE ICES TC95. The same configurations are used even in this study. The total antenna input power was normalized to 10 mW in this study.

1) HALF-WAVELENGTH DIPOLE ANTENNA

Fig. 1 (a) illustrates a half-wavelength dipole modeled as perfect electric conductor. Dipoles working at 10, 30, 60, and 90 GHz were designed. For most of organizations, the antenna was resonated with an adjusted length to obtain

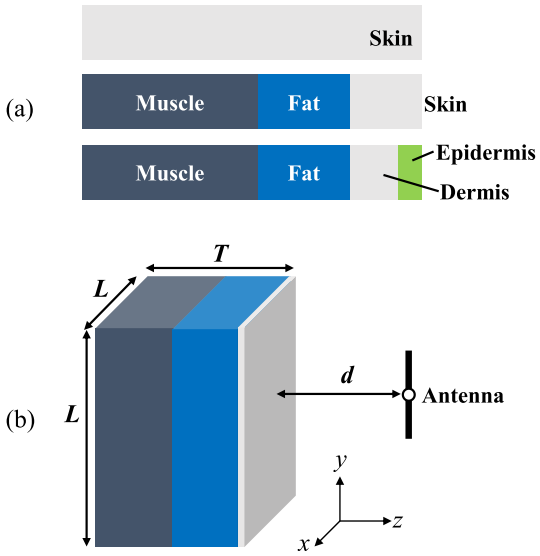

FIGURE 2. Skin models for dosimetry analysis: (a) skin models with different tissue compositions; (b) exposure condition.

the maximum radiation power emitted from the antenna as possible. Table 2 summarizes the dipole length used by each organization.

2) DIPOLE ARRAY ANTENNA

4-by-4 dipole antenna arrays working at frequencies of 10, 30, 60, and 90 GHz have been studied (see Fig. 1 (b)). The same length, as listed in Table 2, was used by the corresponding organization for the dipole element in the array. The separation distance between the feeding points of any two adjacent dipole elements was λ/2, where λ represents the free-space wavelength.

3) PATCH ARRAY ANTENNA

The dimension of a square patch array at 30 GHz is shown in Fig. 1 (c). The patch array has a 100 mm × 100 mm × 0.6 mm dielectric substrate with ε_r of 2.2. The length of the patch element is 0.3λ(i.e. 3 mm at 30 GHz), whereas the separation distance between adjacent patch elements is 0.5λ (i.e. 5 mm at 30 GHz).

4) SLOT ARRAY ANTENNA

A pyramidal horn loaded with a slot array operating at 30 GHz is shown in Fig. 1 (d). The slot array consisted of 6 × 7 rectangular slots symmetrically arranged on the horn aperture and was fabricated in a 0.15-mm-thick stainless steel sheet. The antenna is one of the standardized system validation sources specified in IEC/IEEE [34]–[36].

C. SKIN MODELS AND PARAMETERS

Three stratified skin models were used in this study for dosimetry analysis. Variations in the inner tissue composition are illustrated in Fig. 2 (a). The dimensions of the skin models

TABLE 2. Lengths of dipole antenna elements for each organization.

Org.	10 GHz [mm]	30 GHz [mm]	60 GHz [mm]	90 GHz [mm]
O1	13.6	4.4	2.2	N/A
O2	13.5	4.25	2.125	1.3
O3	13.5	4.75	2.375	1.5
O4	15.0	5.0	2.5	N/A
O5	13.6	4.53	2.27	1.51
O6	15.0	5.0	2.5	1.67

Abbreviations: Organization (Org.).

TABLE 3. Dimension of skin models for each organization.

Org.	Dimension	10 GHz	30 GHz	60 GHz	90 GHz
O1	L [mm]	100	100	50	N/A
	T [mm]	20	20	20	N/A
O2	L [mm]	400	200	100	80
	T [mm]	30	30	30	30
O3 O6	L [mm]	100	50	50	50
	T [mm]	20	20	20	20
O4	L [mm]	200	150	80	N/A
	T [mm]	100	50	40	N/A
O5	L [mm]	200	150	100	60
	T [mm]	100	75	50	30

are $L \times L \times T$ (mm^3), as illustrated in Fig. 2 (b), and are summarized in Table 3. The dielectric properties of tissues obtained by a four-Cole–Cole dispersion model [37]–[39] were used, except for the four-layer skin model [40]–[42], which used independent measurement data. The thicknesses and thermal properties of each tissue layer in the human block models are summarized in Table 4.

D. COMPUTATION OF ELECTROMAGNETIC FIELD

Several numerical techniques have been used to evaluate the IPD in free space and the specific absorption rate (SAR) inside the simplified human block models. Specifically, the finite-difference time-domain (FDTD) method has been adopted by four organizations [43], whereas the finite integration technique (FIT) [44] and the Galerkin-Bubnov indirect boundary element method (GB-IBEM) [45] have been used separately by the two other organizations. Depending on the adopted numerical techniques, different boundary conditions (BCs) have been used to truncate the computational domain. Perfect matched layers have been used as absorbing BCs to suppress (or minimize) reflections of EMF at the boundaries of the computational domain. The numerical methods and spatial resolution in simulations are summarized in Table 5.

TABLE 4. Tissue thicknesses (t) and thermal properties using different Skin Models by each organization.

Org.	Tissue	Thic. [mm]	k [W/(m·°C)]	B [W/(m^3·°C)]	ρ [kg/(m^3)]
O1 (four-layer)	Epi-dermis	0.2	0.45	0	1,109
	Dermis	1.0	0.42	9,100	1,109
	Fat	3.8	0.25	1,700	911
	Muscle	15.0	0.5	2,700	1,090
O2 (three-layer)	Skin	2	0.42	7,441	1,125
	Fat	12	0.25	1,903	916
	Muscle	16	0.5	2,691	1,047
O3 (three-layer)	Skin	1.5	0.37	7,441	1,109
	Fat	4	0.21	1,903	911
	Muscle	14.5	0.49	2,691	1,090
O4 (one-layer)	Skin	T4[(1)]	0.293	9,100	1,100
O5 (one-layer)	Skin	T6[(2)]	0.37	2,230	1,100
O6 (three-layer)	Skin	1.5	0.42	9,100	1,109
	Fat	4	0.25	1,700	911
	Muscle	14.5	0.5	2,700	1,090

Abbreviations: Thickness (Thic.);

[(1)]*T4 = 100 mm @ 10 GHz; 50 mm @ 30 GHz; 40 mm @ 60 GHz;*

[(2)]*T6 = 100 mm @ 10 GHz; 75 mm @ 30 GHz; 50mm @ 60 GHz; 30mm @ 90 GHz.*

TABLE 5. Numerical method and spatial resolution for numerical simulation by each organization.

Org.	Method	Res.	10 GHz	30 GHz	60 GHz	90 GHz
O1	FDTD	Δ [mm]	0.2	0.2	0.1	N/A
O2	FDTD	Δ [mm]	0.5	0.25	0.125	0.1
O3	FDTD	Δ [mm]	0.5	0.25	0.125	0.1
O4	FIT	Δ [mm]	0.15–1.6	0.1–0.75	0.05–0.3	N/A
O5	FDTD	Δ [mm]	0.5	0.25	0.125	0.0625
O6	GB-IBEM	Δ [mm]	0.25	0.25	0.25	0.25

Abbreviations: Resolution (Res.).

Each organization performed two separate EM calculations for each modeling scenario. First, the IPD in free space was calculated without the presence of the body. Then, the simplified human block model was introduced (Section II-C), and electric field strengths in tissue were calculated. In this latter case, the SAR, which is the input parameter for evaluating temperature increase, has been calculated using the

well-known expression of Eq. (1):

$$SAR\,(\boldsymbol{r}) = \frac{\sigma\,(\boldsymbol{r})}{2\rho\,(\boldsymbol{r})}\,|\boldsymbol{E}\,(\boldsymbol{r})|^2\,, \tag{1}$$

where σ represents the tissue conductivity (S/m), and ρ, the mass density (kg/m^3). $\boldsymbol{r}$ denotes the position vector, and $\boldsymbol{E}$ denotes the complex electric field inside the body.

E. THERMAL COMPUTATION

Thermal calculations have been performed to obtain the time-varying tissue temperature (T) by solving the Pennes Bio-Heat Equation (PBHE) [46]–[51], as expressed by Eq. (2):

$$\begin{aligned} c\,(\boldsymbol{r})\,\rho\,(\boldsymbol{r})\,\frac{\partial T\,(\boldsymbol{r},t)}{\partial t} \\ = \nabla\cdot[\kappa\,(\boldsymbol{r})\cdot\nabla T\,(\boldsymbol{r},t)] + \rho\,(\boldsymbol{r})\,SAR\,(\boldsymbol{r}) \\ +\mathrm{A}\,(\boldsymbol{r},t) - B\,(\boldsymbol{r},t)\left[T\,(\boldsymbol{r},t) - T_b\,(\boldsymbol{r},t)\right], \end{aligned} \tag{2}$$

where T and T_b represent temperatures of human tissues and blood (°C), respectively. κ and c represent the thermal conductivity (W/(m K)) and heat capacity (J/(kg K)), respectively. A and B denote the basal metabolism per unit volume (W/m^3) and a term associated with blood flow (W/(m^{3}K)), respectively.

At a steady state, the temperature elevation (ΔT) can be solved using Eq. (3):

$$\begin{aligned} 0 = \nabla\cdot[\kappa\,(\boldsymbol{r})\cdot\nabla\Delta T\,(\boldsymbol{r})] + \rho\,(\boldsymbol{r})\,SAR\,(\boldsymbol{r}) \\ -B\,(\boldsymbol{r},t)\,\Delta T\,(\boldsymbol{r})\,. \end{aligned} \tag{3}$$

Note that the coefficient representing the basal metabolism of the body does not affect the temperature increase caused by EMF exposure when thermoregulatory responses are ignored, as considered in this study. The boundary condition for PBHE describing the heat exchange between air and the skin tissue is given by Eq. (4):

$$-\kappa\,(\boldsymbol{r})\,\frac{\partial T\,(\boldsymbol{r},t)}{\partial \boldsymbol{n}} = h\times[T_{\mathrm{surf}}\,(\boldsymbol{r},t) - T_{\mathrm{air}}\,(t)]\,, \tag{4}$$

where h, T_{surf}, and T_{air} denote the heat transfer coefficient (W/(m^{2}K)), the surface temperature of the tissue (°C), and air temperature (°C), respectively, and $\boldsymbol{n}$ represents the normal vector component at the boundary surface. Instead, adiabatic BCs were assigned to all inner boundaries, which are given by the following equation:

$$\frac{\partial T\,(\boldsymbol{r},t)}{\partial \boldsymbol{n}} = 0. \tag{5}$$

F. METRICS AND POST-PROCESSING METHODS

In this study, two definitions of the spatial-average power density (*s*PD) for the EMF were examined in the absence of the human body. The first is the spatial average of the normal component of the time-averaged PD, as defined by Eq. (6). The second is the spatial average of the norm of the time-averaged PD, as defined by Eq. (7), which considers all three components of the Poynting vector.

$$s\mathrm{PD_n} = \frac{1}{2A}\iint_A \mathrm{Re}\left[\boldsymbol{E}\times\boldsymbol{H}^*\right]\cdot\boldsymbol{n}dA \tag{6}$$

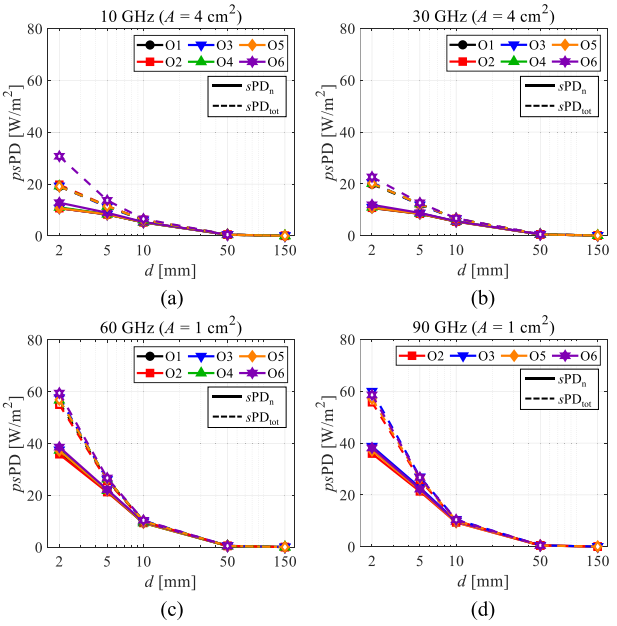

FIGURE 3. Spatially averaged incident power densities as functions of the antenna-to-skin separation distance using half-wavelength dipoles at frequencies of (a) 10 GHz, (b) 30 GHz, (c) 60 GHz, and (d) 90 GHz.

$$s\mathrm{PD_{tot}} = \frac{1}{2A}\iint_A \left|\left|\mathrm{Re}\left[\boldsymbol{E}\times\boldsymbol{H}^*\right]\right|\right| dA \tag{7}$$

$\boldsymbol{E}$ and $\boldsymbol{H}$ denote the complex electric field and magnetic field vectors, respectively; * denotes the complex conjugate; A represents the averaging area; and $\boldsymbol{n}$ represents the unit vector normal to the evaluation plane. Then, the heating factor (*HF*), which is defined as the ratio of the peak steady-state temperature rise ($p\Delta T$) at the skin surface calculated using the assumed thermal parameters to the peak spatial-average PD (*ps*PD) [14], was computed using Eq. (8):

$$HF = \frac{p\Delta T}{psPD}. \tag{8}$$

The corresponding definitions of *HFs* hereafter are denoted as HF_{n} ($p\Delta T/ps\mathrm{PD_n}$) and HF_{tot} ($p\Delta T/ps\mathrm{PD_{tot}}$).

III. INTERCOMPARISON RESULTS

This section presents the intercomparison results in terms of peak spatial-average IPD and *HF*s using different antennas. The intercomparison plots of $ps\mathrm{PD_n}$ and $ps\mathrm{PD_{tot}}$, as well as HF_{n} and HF_{tot}, were averaged over an area of $A = 4$ cm^2 at 6–30 GHz and $A = 1$ cm^2 above 30 GHz. The antenna-to-skin separation distance varied from 2 to 150 mm.

A. COMPARISON OF PEAK SPATIAL-AVERAGE INCIDENT POWER DENSITY

Figures 3 and 4 show the intercomparison results of *ps*PD as a function of the antenna-to-skin separation distance d exposed to the single dipole and the 4 × 4 dipole array antenna for the exposure scenarios in Table 1, respectively, at a frequency from 10 to 90 GHz. The lines with solid markers indicate

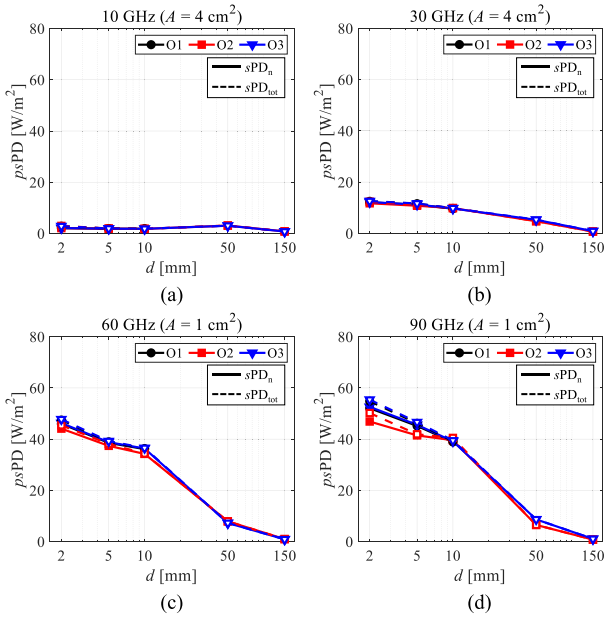

FIGURE 4. Spatially averaged incident power densities as functions of the antenna-to-skin separation distance using 4 × 4 dipole arrays at frequencies of (a) 10 GHz, (b) 30 GHz, (c) 60 GHz, and (d) 90 GHz.

the results of $psPD_n$, whereas the dashed lines with empty markers denote the results of $psPD_{tot}$.

In Fig. 3, both $psPD_n$ and $psPD_{tot}$ decrease monotonically with an increase in the separation distance d. $psPD_{tot}$ is greater than $psPD_n$ in the 2–150 mm range. In the 2–5 mm range, an obvious difference between $psPD_n$ and $psPD_{tot}$ is observed, where the maximum absolute difference between $psPD_n$ and $psPD_{tot}$ is up to 3.8 dB at 10 GHz when $d = 2$ mm. At $d > 5$ mm, however, the corresponding difference decreases to less than 1 dB and approaches 0 dB when d increases above 50 mm, which is in the far-field region of a half-wavelength dipole antenna.

By contrast, when the 4 × 4 dipole array is used as an exposure source, as illustrated in Fig. 4, owing to the dispersion of multiple near-field peaks caused by the wave source of the antenna array, the trends of $psPD$s completely differ from those of the dipoles illustrated in Fig. 3. In addition, the absolute difference between $psPD_n$ and $psPD_{tot}$ is significantly reduced for cases of the 4 × 4 dipole array; the maximum absolute difference at $d = 2$ mm is reduced to less than 1.5 dB at 10 GHz, and it is not greater than 0.1 dB when d is greater than 5 mm. The above results indicate that at a separation distance $d > 5$ mm, there is no obvious discrepancy between $psPD_n$ and $psPD_{tot}$ for either case of dipole or dipole array source.

Tables 6 and 7 present the statistical mean value and standard deviation of $psPD_n$ and $psPD_{tot}$ of the numerical results from the six organizations for cases of the dipole and dipole array, respectively. The separation distances from the antenna for cases at $d = 2$, 5, and 10 mm were compared. Hereafter, we evaluate the relative standard deviation (RSD), which is defined as the ratio of standard deviation to the mean value, as a metric for intercomparison of different research groups.

TABLE 6. Mean value and standard deviation of spatially averaged incident power densities using dipole antennas.

Peak Spatial-Average IPD	Frequency [GHz]	d = 2 mm	d = 5 mm	d = 10 mm
$psPD_n$ [W/m^2]	10	11.13 ± 0.85	8.43 ± 0.25	5.28 ± 0.05
	30	11.01 ± 0.46	8.56 ± 0.14	5.48 ± 0.06
	60	37.19 ± 0.94	21.84 ± 0.35	9.49 ± 0.15
	90	37.48 ± 1.23	22.09 ± 0.63	9.6 ± 0.26
$psPD_{tot}$ [W/m^2]	10	21.19 ± 4.68	11.81 ± 0.95	6.24 ± 0.16
	30	20.6 ± 1.04	12.2 ± 0.27	6.55 ± 0.07
	60	56.93 ± 1.54	26.13 ± 0.39	10.14 ± 0.16
	90	57.85 ± 1.83	26.44 ± 0.51	10.26 ± 0.26

TABLE 7. Mean values and standard deviations of spatially averaged incident power densities using dipole array antennas.

Peak Spatial-Average IPD	Frequency [GHz]	d = 2 mm	d = 5 mm	d = 10 mm
$psPD_n$ [W/m^2]	10	2.12 ± 0.01	1.87 ± 0.004	1.82 ± 0.01
	30	12.01 ± 0.25	11.06 ± 0.26	9.73 ± 0.11
	60	45.46 ± 1.18	38.25 ± 0.76	35.57 ± 1.16
	90	50.53 ± 3.17	44.07 ± 2.27	39.21 ± 0.35
$psPD_{tot}$ [W/m^2]	10	2.9 ± 0.06	1.95 ± 0.01	1.85 ± 0.01
	30	12.48 ± 0.13	11.48 ± 0.25	9.81 ± 0.08
	60	46.87 ± 1.29	38.78 ± 0.57	35.76 ± 1.19
	90	53.47 ± 2.85	44.91 ± 2.61	39.73 ± 0.67

For the case of the dipole source, as presented in Table 6, the maximum RSD of $psPD_n$ and $psPD_{tot}$ is 7.6% and 22.1%, respectively, at the frequency of 10 GHz when $d = 2$ mm. At $d > 5$ mm, the RSD of $psPD_n$ and $psPD_{tot}$ is less than 3% and 8.1% and does not exceed 1.0% and 2.6%, respectively, when the separation distance d increases to 10 mm.

By contrast, for the case of the 4 × 4 dipole array, as presented in Table 7, the maximum RSD is nonexistent at 10 GHz

TABLE 8. Mean values and standard deviations of heating factors using dipole antennas.

Heating factors	Frequency [GHz]	d = 2 mm	d = 5 mm	d = 10 mm
HF_{n} [°C/W/m^2]	10	0.0632 ± 0.0219	0.0147 ± 0.0062	0.0061 ± 0.0024
	30	0.0447 ± 0.019	0.0213 ± 0.0054	0.0131 ± 0.0033
	60	0.0142 ± 0.0033	0.0102 ± 0.0027	0.0092 ± 0.0024
	90	0.0233 ± 0.0059	0.0125 ± 0.0031	0.0113 ± 0.0021
HF_{tot} [°C/W/m^2]	10	0.0335 ± 0.0118	0.0106 ± 0.0046	0.0052 ± 0.002
	30	0.0239 ± 0.0102	0.0149 ± 0.0037	0.0109 ± 0.0028
	60	0.0093 ± 0.0021	0.0085 ± 0.0023	0.0086 ± 0.0022
	90	0.0151 ± 0.0039	0.0104 ± 0.0025	0.0105 ± 0.0019

TABLE 9. Mean value and standard deviation of heating factors using dipole array antennas.

Heating factors	Frequency [GHz]	d = 2 mm	d = 5 mm	d = 10 mm
HF_{n} [°C/W/m^2]	10	0.0208 ± 0.003	0.005 ± 0.0012	0.0042 ± 0.0017
	30	0.006 ± 0.0007	0.0265 ± 0.003	0.0221 ± 0.0034
	60	0.0077 ± 0.0001	0.0167 ± 0.0025	0.0138 ± 0.0046
	90	0.0192 ± 0.006	0.0257 ± 0.0045	0.0183 ± 0.0014
HF_{tot} [°C/W/m^2]	10	0.0153 ± 0.0021	0.0048 ± 0.0012	0.0041 ± 0.0017
	30	0.0057 ± 0.0006	0.0255 ± 0.0029	0.0219 ± 0.0033
	60	0.0074 ± 0.0001	0.0165 ± 0.0025	0.0137 ± 0.0046
	90	0.0181 ± 0.0055	0.0252 ± 0.0046	0.0181 ± 0.0016

when $d = 2$ mm. For both cases of $ps\mathrm{PD_n}$ and $ps\mathrm{PD_{tot}}$, the maximum RSD is approximately 6.3% ($d = 2$ mm) and 5.8% ($d = 5$ mm), respectively, at the frequency of 90 GHz. The maximum RSD of the dipole arrays decreases significantly compared to that of the dipole sources. When d increases to 10 mm, the corresponding maximum RSD for each $ps\mathrm{PD_n}$ and $ps\mathrm{PD_{tot}}$ is less than 3.3%.

The above results indicate that for the EMF calculation in the antenna near-field, such as the extreme case of $d = 2$ mm, there will be noticeable differences in the results from the different organizations, especially for cases of $ps\mathrm{PD_{tot}}$. At a separation distance $d > 5$ mm, however, the difference in both $ps\mathrm{PD_n}$ and $ps\mathrm{PD_{tot}}$ for all cases of the dipole and dipole array is less than 8.1%. When one considers the different numerical methods used by each organization, this difference is relatively small.

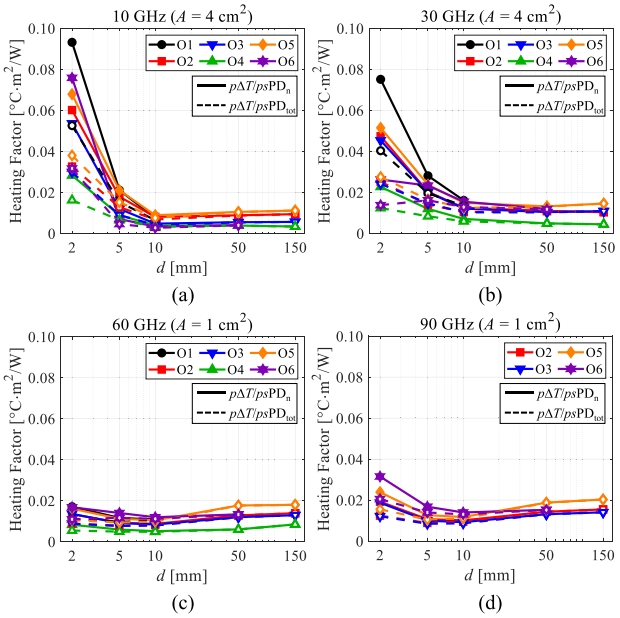

FIGURE 5. Heating factors of $s\mathrm{PD_n}$ and $s\mathrm{PD_{tot}}$ as functions of the antenna-to-skin separation distance using half-wavelength dipoles at frequencies of (a) 10 GHz, (b) 30 GHz, (c) 60 GHz, and (d) 90 GHz.

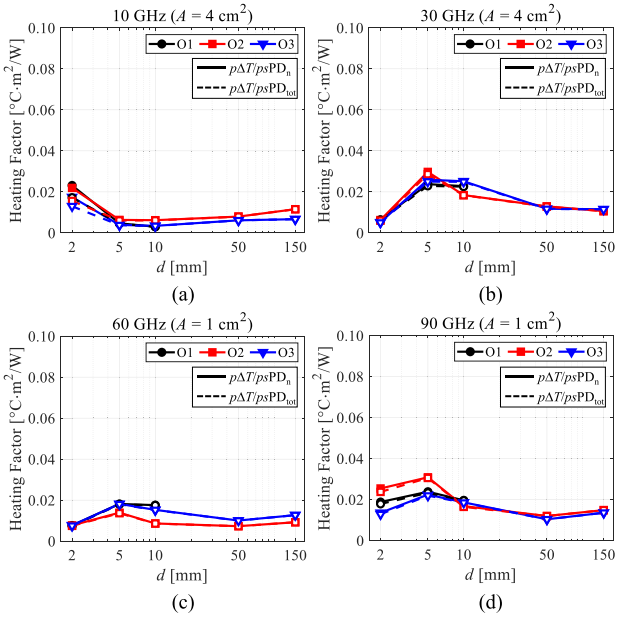

FIGURE 6. Heating factors of $s\mathrm{PD_n}$ and $s\mathrm{PD_{tot}}$ as functions of the antenna-to-skin separation distance using 4 × 4 dipole arrays at frequencies of (a) 10 GHz, (b) 30 GHz, (c) 60 GHz, and (d) 90 GHz.

B. COMPARISON OF HEATING FACTORS

Figures 5 and 6 show the intercomparison results of the HFs as functions of the antenna-to-skin separation distance

d exposed to the radiation sources of the dipole and the 4 × 4 dipole array, respectively. In Figs. 5 and 6, the lines with solid markers indicate the results of HF_{n}, whereas the dashed lines with empty markers denote those of HF_{tot}.

In Fig. 5, at frequencies of 10 and 30 GHz when $d = 2$ mm, a significant increase in *HFs* is observed. As d increases to 10 mm, the profiles of HF_{n} and HF_{tot} at 10 and 30 GHz decrease gradually. By contrast, the results of *HFs* at 60 and 90 GHz show a relatively gentle trend of variation from 2 to 150 mm. By contrast, the deviation between HF_{n} and HF_{tot} in the range of 2 to 5 mm is up to 58% (3.8 dB) at 10 GHz. At $d > 5$ mm, the difference decreases to less than 20% (1 dB), and almost no difference is observed when d increases above 50 mm, corresponding to the results mentioned in Section III-A.

When the 4 × 4 dipole array is used, as shown in Fig. 6, the entire difference between HF_{n} and HF_{tot} decreases significantly compared to the dipole source shown in Fig. 5, owing to the dispersion of the near-field distribution of the dipole array. The maximum difference between HF_{n} and HF_{tot} at $d = 2$ mm is less than 29% (1.5 dB) and does not exceed 2% (0.1 dB) when d is greater than 5 mm.

Fig. 7 shows the distributions of $s\mathrm{PD}_{\mathrm{n}}$, $s\mathrm{PD}_{\mathrm{tot}}$ and ΔT for dipole and dipole array antenna at 30 GHz when d is 2, 5, and 10 mm. The area for spatial average of IPD were set to 1 and 4 cm^2, respectively. For simplicity, we have selected the results of the first three organizations (O1, O2, and O3) that provided all the data of dipole and dipole array, as shown in Figs. 7 (a) and (b), respectively. In Fig. 7, for each research organization, the distributions of using dipole array antennas show higher locality compared to those of using single dipoles. When the antenna-skin separation distance d is larger than 2 mm, there is no large obvious difference in the distributions between the two definitions of IPD.

Tables 8 and 9 list the statistical mean values and standard deviations of the HF_{n} and HF_{tot} of the numerical results from the six organizations for cases of the dipole and the dipole array, respectively. For the case of the dipole source, as presented in Table 8, the maximum RSD of HF_{n} and HF_{tot} is 42.5% and 43.2%, which occurred at frequencies of 30 GHz when $d = 2$ mm and 10 GHz when $d = 5$ mm, respectively. The corresponding maximum RSD is less than 38.7% and 39%, respectively, when $d = 10$ mm.

For the case of the 4 × 4 dipole array, as presented in Table 9, the maximum RSD of HF_{n} and HF_{tot} decreases to approximately 31% and 30%, respectively, at a frequency of 90 GHz when $d = 2$ mm. At $d = 5$ mm, the corresponding RSD of HF_{n} and HF_{tot} further decreases to less than 25% and 24.5%, respectively, at a frequency of 10 GHz but increases up to 41.2% for both HF_{n} and HF_{tot} at 10 GHz when d increases to 10 mm.

The above results indicate that there is no obvious difference between HF_{n} and HF_{tot} when the antenna-to-model separation distance is greater than 5 mm. However, the difference in *HFs* from six organizations is relatively greater than that in *ps*PD, indicating that a difference in the numerical analysis of temperature rise among various organizations may exist, as different skin models have been used.

TABLE 10. Difference in Heating factors due to different models and their dielectric/thermal parameters using half-wavelength dipoles at 10 GHz replicated by organization 2.

Org.	HF_{n} avg.1	HF_{tot} avg.1	HF_{n} avg.4	HF_{tot} avg.4
O1	−12.6%	−12.2%	−12.7%	−12.1%
O2 (ref.)	-	-	-	-
O3	−10.9%	−10.1%	−10.8%	−8.2%
O4	−4.5%	−4.3%	−6.2%	−5.4%
O5	0.0%	0.8%	−0.3%	1.3%
O6	−30.0%	−31.3%	−30.9%	−33.1%

C. VARIABILITY OF BODY MODEL AND THERMAL PARAMETER

Several body models with different tissue compositions were used in the working group's intercomparison study. A previous study examined variabilities related to tissue thickness in a multi-layer model using the Monte Carlo method [41]. In this section, the variability in the calculated *HFs* caused by different body models and thermal parameters is further assessed. To avoid the discrepancies caused by the numerical methods, the computation is performed by organization 2 using the dipole source at frequencies of 10 and 30 GHz with their original code based on the following conditions:

- the same resolution and model structure,
- the same dielectric and thermal parameters,
- distance between the antenna and the model $d = 10$ mm, and
- the same antenna length: 13.25–13.5 mm (10 GHz) and 4.1–4.25 mm (30 GHz).

Note that the antenna length was adjusted in consideration of the difference in resolution used by each organization. The comparisons of *HFs* between organization 2 and other organizations are summarized in Table 10 for 10 GHz and Table 11 for 30 GHz, respectively. As presented in Tables 10 and 11, the maximum difference observed at 10 and 30 GHz is 33.1% and 19.6%, respectively, compared to those of organization 2. The corresponding difference with other organizations is less than 12.7% and 17.6%, respectively. The global differences can be considered acceptable, indicating that the deviation for dosimetry analysis caused by the difference in body models and dielectric/thermal parameters is insignificant.

D. VARIABILITY OF ANTENNA MODEL

The variations in RSD between different organizations in previous sections indicate that the *HF* may be affected by the antennas used. In this section, the variability caused by the antenna models was investigated.

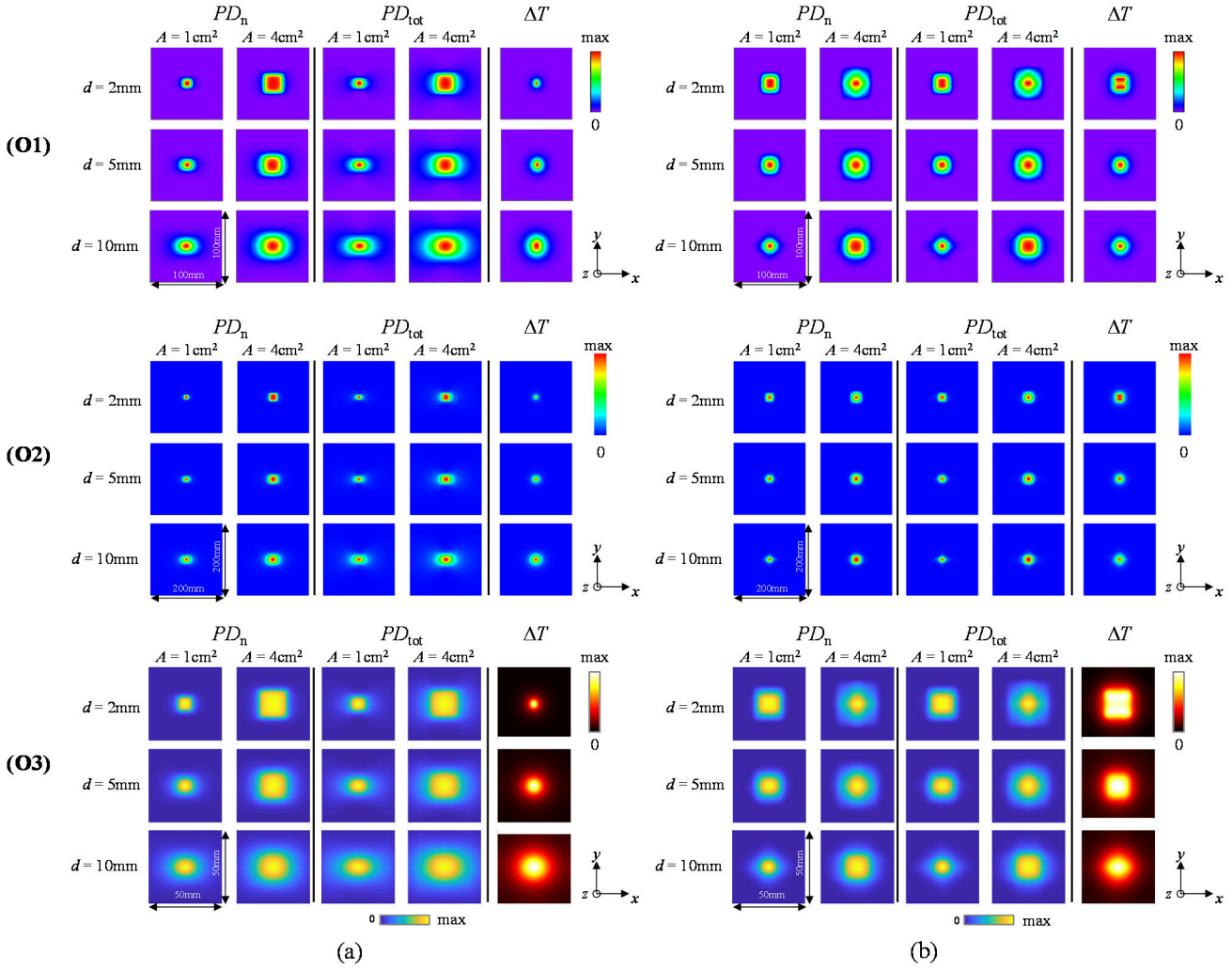

FIGURE 7. Distributions of spatially averaged incident power densities and surface temperature elevation for dipole and dipole array antennas at 30 GHz with antenna-skin separation distance of 2, 5, and 10 mm from different organizations: (a) dipole, (b) dipole array.

TABLE 11. Difference in Heating factors due to different models and their dielectric/thermal parameters using half-wavelength dipoles at 30 GHz replicated by organization 2.

Org.	HF_n avg.1	HF_{tot} avg.1	HF_n avg.4	HF_{tot} avg.4
O1	16.6%	17.1%	16.8%	17.6%
O2 (ref.)	-	-	-	-
O3	−14.7%	−14.0%	−14.7%	−12.4%
O4	4.9%	5.0%	3.7%	3.9%
O5	8.6%	9.3%	8.3%	9.2%
O6	18.9%	19.6%	18.7%	19.4%

Fig. 8 shows the *HF*s of *ps*PD using the antenna models, namely half-wavelength dipole, the 4 × 4 dipole array, the 4 × 4 patch array, and the pyramidal horn with a 6 × 7 slot array at 30 GHz, as illustrated in Fig. 1 (d). The spatial averaging area was set to $A = 4$ cm^2. The results at the separation distance of $d = 2$, 5, and 10 mm were compared. The error bars show the statistical mean value and the standard deviation of *HF*s from different organizations. The results of HF_n and HF_{tot} are illustrated in Figs. 8 (a) and (b), respectively.

As illustrated in Fig. 8, for each antenna model, except for the dipole array, the standard deviations increase markedly at $d = 2$ mm compared with those at other separation distances. In Fig. 8 (a), the maximum RSD of HF_n is 42.5%, 11.4%, 32.7%, and 58.6% for the case of the dipole, dipole array, patch array, and slot array, respectively, when $d = 2$ mm. The corresponding RSD of HF_{tot} is 42.6%, 11%, 31.7%, and 60.3%, respectively, as illustrated in Fig. 8 (b). At $d = 5$ mm, the maximum RSD decreases to less than 26.3% and does not exceed 25.5% at $d = 10$ mm, indicating a fair agreement across the different sets of results when d is greater than 5 mm. The overall level of deviation of *HF*s due to different antenna models at 30 GHz is comparable with those

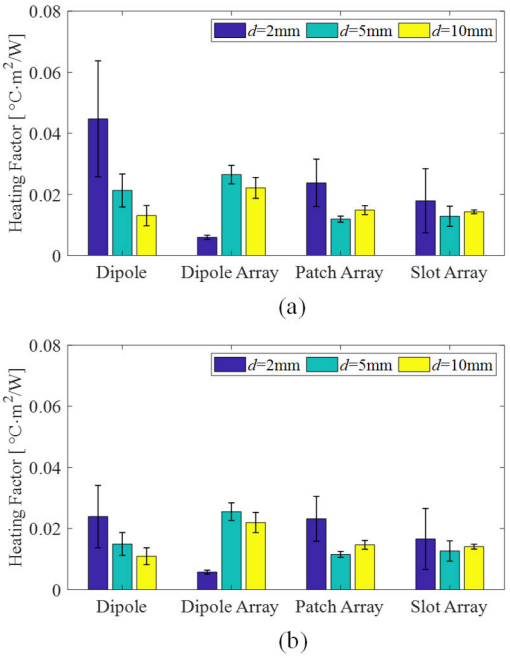

FIGURE 8. Heating factors of sPD_n and sPD_{tot} using different antennas at 30 GHz with an averaging area of $A = 4$ cm^2: (a) HF_n; (b) HF_{tot}.

mentioned in Section III-B, demonstrating a slight dependency of the antenna model for numerical computation errors in the dosimetry analysis. The relatively large RSD for the case of the slot array can be attributed to the fact that only two organizations provided related results for intercomparison in this case, which may result in an increase in deviation due to the insufficient data for statistical analysis.

IV. DISCUSSION AND CONCLUSION

As mentioned above, we establish exposure scenarios considering product safety in which a worst-case exposure is assumed and exposure guidelines/standards in which more practical consideration is included. In exposure guidelines/standards, some practical consideration is given. IEEE C95.1-2019 states that "*the safety limits for electrostimulation are based on conservative assumptions of exposure; however, they cannot address every conceivable assumption.*" Thus, our approximation is still useful for providing general intercomparison and interpreting the results. For a distance less than 5 mm, a potential application would be a body-worn wireless device. In such cases, the antenna would be supported by the metallic plate to avoid the interaction and maintain the antenna impedance. The misuse (e.g., incorrect orientation) of the antenna would be considered for product safety in general, rather than the EMF safety. Note that, in general, the output power of wearable devices would be sufficiently small, and the antenna type might be different from those considered in this study.

In exposure scenarios, especially for an antenna-to-model separation distance less than 5 mm, some hotspots were observed only beneath the antenna feeding point for dipole or dipole array antennas. The size of the focal area is comparable to the separation between two linear conductors, depending on the modeling of the feeding point. Note that this is not caused by the beam formation of multiple antennas or antenna arrays. When an antenna array was considered, the number of such focal points coincided with that of antenna elements, and the increase in the *HF* was thus insignificant when the separation between array elements was considered.

This study made the first intercomparison of calculated spatially averaged IPD and resultant temperature rise in a simplified body model for exposure from different antennas ranging from 10 to 90 GHz. The main causes of numerical calculation errors in the dosimetry analysis using various skin and antenna models were investigated using objective comparison of analysis results from six different research groups. The intercomparison results indicate that the maximum RSD of spatially averaged incident power densities is less than 22.1% and 6.3% for the dipole antenna and the dipole array, respectively. In addition, the maximum RSD of the *HF*, which is defined as the ratio of peak temperature elevation at the skin surface to peak spatially averaged IPD, does not exceed 43.2% and 41.2% for cases of the dipole antenna and the dipole array, respectively. Although there is a slight dependency on the body model, thermal parameters, and antenna models, the deviation of *HF*s is insignificant when one considers the numerical methods used by different organizations. The fair agreement among the intercomparison results demonstrates that numerical calculation errors of dosimetry analysis caused by the definition of spatially averaged IPD are marginal. By contrast, some other factors, such as the antenna type, the separation distance between the antenna and the body model, and the numerical method, may result in relatively large discrepancies.

REFERENCES

[1] International Commission on Non-Ionizing Radiation Protection, "Guidelines for limiting exposure to electromagnetic fields (100 kHz to 300 GHz)," *Health Phys.*, vol. 118, no. 5, pp. 483–524, May 2020.

[2] *IEEE Standard for Safety Levels With Respect to Human Exposure to Electric, Magnetic and Electromagnetic Fields*, Standard IEEE-C95.1, 0 Hz to 300 GHz, 2019.

[3] Y. Diao, E. A. Rashed, and A. Hirata, "Assessment of absorbed power density and temperature rise for nonplanar body model under electromagnetic exposure above 6 GHz," *Phys. Med. Biol.*, vol. 65, no. 22, Nov. 2020, Art. no. 224001.

[4] D. Funahashi, A. Hirata, S. Kodera, and K. R. Foster, "Area-averaged transmitted power density at skin surface as metric to estimate surface temperature elevation," *IEEE Access*, vol. 6, pp. 77665–77674, 2018.

[5] The International Commission on Non-Ionizing Radiation Protection, "Guidelines for limiting exposure to time-varying electric, magnetic, and electromagnetic fields (up to 300 GHz)," *Health Phys.*, vol. 74, no. 4, pp. 494–522, Apr. 1998.

[6] *IEEE Standard for Safety Levels With Respect to Human Exposure to Radio Frequency Electromagnetic Fields, 3 kHz to 300 GHz*, Standard C95.1, 2005.

[7] A. Hirata, Y. Diao, T. Onishi, K. Sasaki, S. Ahn, D. Colombi, V. De Santis, I. Laakso, L. Giaccone, J. Wout, E. Rashed, W. Kainz, and J. Chen, "Assessment of human exposure to electromagnetic fields: Review and future directions," *IEEE Trans. Electromagn. Compat.*, vol. 63, no. 5, pp. 1619–1630, Oct. 2021.

[8] S. I. Alekseev, A. A. Radzievsky, M. K. Logani, and M. C. Ziskin, "Millimeter wave dosimetry of human skin," *Bioelectromagnetics*, vol. 29, no. 1, pp. 65–70, Jan. 2008.
[9] M. C. Ziskin, S. I. Alekseev, K. R. Foster, and Q. Balzano, "Tissue models for RF exposure evaluation at frequencies above 6 GHz," *Bioelectromagnetics*, vol. 39, no. 3, pp. 173–189, Apr. 2018.
[10] K. R. Foster, A. Lozano-Nieto, P. J. Riu, and T. S. Ely, "Heating of tissues by microwaves: A model analysis," *Bioelectromagnetics*, vol. 19, no. 7, pp. 420–428, 1998.
[11] K. R. Foster, M. C. Ziskin, and Q. Balzano, "Thermal modeling for the next generation of radiofrequency exposure limits: Commentary," *Health Phys.*, vol. 113, no. 1, pp. 41–53, 2017.
[12] A. Hirata, "Review on human dosimetry for radio-frequency exposure above 6 GHz-international exposure standards," in *Proc. Asia–Pacific Microw. Conf. (APMC)*, Nov. 2018, pp. 681–683.
[13] A. Hirata, D. Funahashi, and S. Kodera, "Setting exposure guidelines and product safety standards for radio-frequency exposure at frequencies above 6 GHz: Brief review," *Ann. Telecommun.*, vol. 74, nos. 1–2, pp. 17–24, Feb. 2019.
[14] Y. Hashimoto, A. Hirata, R. Morimoto, S. Aonuma, I. Laakso, K. Jokela, and K. R. Foster, "On the averaging area for incident power density for human exposure limits at frequencies over 6 GHz," *Phys. Med. Biol.*, vol. 62, no. 8, pp. 3124–3138, Apr. 2017.
[15] K. Foster and D. Colombi, "Thermal response of tissue to RF exposure from canonical dipoles at frequencies for future mobile communication systems," *Electron. Lett.*, vol. 53, no. 5, pp. 360–362, Mar. 2017.
[16] K. Sasaki, K. Li, J. Chakarothai, T. Iyama, T. Onishi, and S. Watanabe, "Error analysis of a near-field reconstruction technique based on plane wave spectrum expansion for power density assessment above 6 GHz," *IEEE Access*, vol. 7, pp. 11591–11598, 2019.
[17] S. Omi, K. Sasaki, and K. Wake, "Performance analysis of incident power density evaluation by inverse source method for compliance assessment at quasi-millimeter and millimeter wave bands," *IEEE Trans. Electromagn. Compat.*, vol. 63, no. 5, pp. 1649–1657, Oct. 2021.
[18] Y. Diao and A. Hirata, "Exposure assessment of array antennas at 28 GHz using hybrid spherical near-field transformation and FDTD method," *IEEE Trans. Electromagn. Compat.*, vol. 63, no. 5, pp. 1690–1698, Oct. 2021.
[19] W. He, B. Xu, M. Gustafsson, Z. Ying, and S. He, "RF compliance study of temperature elevation in human head model around 28 GHz for 5G user equipment application: Simulation analysis," *IEEE Access*, vol. 6, pp. 830–838, 2018.
[20] W. He, B. Xu, Y. Yao, D. Colombi, Z. Ying, and S. He, "Implications of incident power density limits on power and EIRP levels of 5G millimeter-wave user equipment," *IEEE Access*, vol. 8, pp. 148214–148225, 2020.
[21] B. Xu, K. Zhao, Z. Ying, D. Sjöberg, W. He, and S. He, "Analysis of impacts of expected RF EMF exposure restrictions on peak EIRP of 5G user equipment at 28 GHz and 39 GHz bands," *IEEE Access*, vol. 7, pp. 20996–21005, 2019.
[22] A. Christ, T. Samaras, E. Neufeld, and N. Kuster, "Limitations of incident power density as a proxy for induced electromagnetic fields," *Bioelectromagnetics*, vol. 41, no. 5, pp. 348–359, May 2020.
[23] D. Colombi, B. Thors, C. TöRnevik, and Q. Balzano, "RF energy absorption by biological tissues in close proximity to mmW 5G wireless equipment," *IEEE Access*, vol. 6, pp. 4974–4981, 2018.
[24] B. Thors, D. Colombi, Z. Ying, T. Bolin, and C. Törnevik, "Exposure to RF EMF from array antennas in 5G mobile communication equipment," *IEEE Access*, vol. 4, pp. 7469–7478, 2016.
[25] E. Carrasco, D. Colombi, K. R. Foster, M. Ziskin, and Q. Balzano, "Exposure assessment of portable wireless devices above 6 GHz," *Radiat. Prot. Dosim.*, vol. 183, no. 4, pp. 489–496, Jun. 2019.
[26] D. Funahashi, T. Ito, A. Hirata, T. Iyama, and T. Onishi, "Averaging area of incident power density for human exposure from patch antenna arrays," *IEICE Trans. Electron.*, vol. E101.C, no. 8, pp. 644–646, Aug. 2018.
[27] T. Nakae, D. Funahashi, J. Higashiyama, T. Onishi, and A. Hirata, "Skin temperature elevation for incident power densities from dipole arrays at 28 GHz," *IEEE Access*, vol. 8, pp. 26863–26871, 2020.
[28] Y. Diao, K. Li, K. Sasaki, S. Kodera, I. Laakso, W. E. Hajj, and A. Hirata, "Effect of incidence angle on the spatial-average of incident power density definition to correlate skin temperature rise for millimeter wave exposures," *IEEE Trans. Electromagn. Compat.*, vol. 63, no. 5, pp. 1709–1716, Oct. 2021.
[29] K. Li, K. Sasaki, S. Watanabe, and H. Shirai, "Relationship between power density and surface temperature elevation for human skin exposure to electromagnetic waves with oblique incidence angle from 6 GHz to 1 THz," *Phys. Med. Biol.*, vol. 64, no. 6, Mar. 2019, Art. no. 065016.
[30] T. Samaras and N. Kuster, "Theoretical evaluation of the power transmitted to the body as a function of angle of incidence and polarization at frequencies >6 GHz and its relevance for standardization," *Bioelectromagnetics*, vol. 40, no. 2, pp. 136–139, Jan. 2019.
[31] A. Hirata, S. Watanabe, O. Fujiwara, M. Kojima, K. Sasaki, and T. Shiozawa, "Temperature elevation in the eye of anatomically based human head models for plane-wave exposures," *Phys. Med. Biol.*, vol. 52, no. 21, pp. 6389–6399, Oct. 2007.
[32] T. Wu, T. S. Rappaport, and C. M. Collins, "Safe for generations to come: Considerations of safety for millimeter waves in wireless communications," *IEEE Microw. Mag.*, vol. 16, no. 2, pp. 65–84, Mar. 2015.
[33] B. B. Beard, W. Kainz, T. Onishi, T. Iyama, S. Watanabe, O. Fujiwara, J. Wang, G. Bit-Babik, A. Faraone, J. Wiart, and A. Christ, "Comparisons of computed mobile phone induced SAR in the SAM phantom to that in anatomically correct models of the human head," *IEEE Trans. Electromagn. Compat.*, vol. 48, no. 2, pp. 397–407, May 2006.
[34] S. Pfeifer, E. Carrasco, P. Crespo-Valero, E. Neufeld, S. Kuhn, T. Samaras, A. Christ, M. H. Capstick, and N. Kuster, "Total field reconstruction in the near field using pseudo-vector E-field measurements," *IEEE Trans. Electromagn. Compat.*, vol. 61, no. 2, pp. 476–486, Apr. 2019.
[35] *Measurement Procedure for the Evaluation of Power Density Related to Human Exposure to Radio Frequency Fields From Wireless Communication Devices Operating Between 6 GHz and 100 GHz*, document IEC TR 63170 ED1, 2018.
[36] *Assessment of Power Density of Human Exposure to Radio Frequency Fields From Wireless Devices in Close Proximity to the Head and Body (Frequency Range of 6 GHz to 300 GHz)*, document IEC/IEEE 63195-1 CDV, 2020.
[37] S. Gabriel, R. W. Lau, and C. Gabriel, "The dielectric properties of biological tissues: III. Parametric models for the dielectric spectrum of tissues," *Phys. Med. Biol.*, vol. 41, no. 11, pp. 2271–2293, 1996.
[38] C. Gabriel, "Compilation of the dielectric properties of body tissues at RF and microwave frequencies," Occupational Environ. Health Directorate Radiofrequency Radiat. Division, Brooks Air Force Base, TX, USA, Tech. Rep. N.AL/OE-TR-1996-0037, 1996.
[39] P. A. Hasgall. (May 15, 2018). *IT'IS Database for Thermal and Electromagnetic Parameters of Biological Tissues, Version 4.0*. [Online]. Available: http://www.itis.swiss/database
[40] K. Sasaki, K. Wake, and S. Watanabe, "Measurement of the dielectric properties of the epidermis and dermis at frequencies from 0.5 GHz to 110 GHz," *Phys. Med. Biol.*, vol. 59, no. 16, pp. 4739–4747, Aug. 2014.
[41] K. Sasaki, M. Mizuno, and K. Wake, "Monte Carlo simulations of skin exposure to electromagnetic field from 10 GHz to 1 THz Monte Carlo simulations of skin exposure to electromagnetic field from 10 GHz to 1 THz," *Phys. Med. Biol.*, vol. 62, pp. 6993–7010, 2017.
[42] K. Sasaki, K. Kawabata, Y. Shimizu, S. Watanabe, K. Wake, R. Suga, and O. Hashimoto, "Design of a skin equivalent phantom for estimating surface temperature elevation due to human exposure to electromagnetic fields from 10 to 100 GHz," *IEEE Trans. Electromagn. Compat.*, vol. 63, no. 5, pp. 1631–1639, Oct. 2021.
[43] A. Taflove and S. C. Hagness, *Computational Electrodynamics: The Finite-Difference Time-Domain Method*, 3rd ed. Norwood, MA, USA: Artech House, 2005.
[44] T. Weiland, "A discretization method for the solution of Maxwell's equations for six-component fields," *Electron. Commun., (AEÜ)*, vol. 31, p. 116, 1977.
[45] D. Poljak, *Advanced Modeling in Computational Electromagnetic Compatibility*. Hoboken, NJ, USA: Wiley, 2007.
[46] H. H. Pennes, "Analysis of tissue and arterial blood temperature in resting forearm," *J. Appl. Physiol.*, vol. 1, pp. 93–122, 1948.
[47] A. Hirata, O. Fujiwara, and T. Shiozawa, "Correlation between peak spatial-average SAR and temperature increase due to antennas attached to human trunk," *IEEE Trans. Biomed. Eng.*, vol. 53, no. 8, pp. 1658–1664, Aug. 2006.
[48] A. Hirata and O. Fujiwara, "The correlation between mass-averaged SAR and temperature elevation in the human head model exposed to RF near-fields from 1 to 6 GHz," *Phys. Med. Biol.*, vol. 54, no. 23, pp. 7227–7238, Dec. 2009.

[49] R. Morimoto, I. Laakso, V. De Santis, and A. Hirata, "Relationship between peak spatial-averaged specific absorption rate and peak temperature elevation in human head in frequency range of 1–30 GHz," *Phys. Med. Biol.*, vol. 61, no. 14, pp. 5406–5425, Jul. 2016.
[50] R. Morimoto, A. Hirata, I. Laakso, M. C. Ziskin, and K. R. Foster, "Time constants for temperature elevation in human models exposed to dipole antennas and beams in the frequency range from 1 to 30 GHz," *Phys. Med. Biol.*, vol. 62, no. 5, pp. 1676–1699, Feb. 2017.
[51] A. Hirata, S. Kodera, K. Sasaki, J. Gomez-Tames, I. Laakso, A. Wood, S. Watanabe, and K. R. Foster, "Human exposure to radiofrequency energy above 6 GHz: Review of computational dosimetry studies," *Phys. Med. Biol.*, vol. 66, no. 8, Apr. 2021, Art. no. 08TR01.

KUN LI (Member, IEEE) received the B.E. degree in communication engineering from the Nanjing University of Posts and Telecommunications, Nanjing, China, in 2011, and the M.E. and Ph.D. degrees in electrical engineering from Toyama University, Toyama, Japan, in 2014 and 2017, respectively.

From 2017 to 2019, he was a Researcher with the Electromagnetic Compatibility Laboratory, National Institute of Information and Communications Technology (NICT), Tokyo, Japan. He is currently an Assistant Professor at Kagawa University, Japan. His research interests include bio-EMC issues on EMF safety, and over-the-air testing for MIMO and body area network systems.

Dr. Li is a member of IEICE. He was a recipient of the Young Scientist Award of the URSI in 2020, the Risaburo Sato Award of EMC Sapporo & AMPEC in 2019, the IEEE AP-S Japan Student Award in 2015, and the IEICE Best Letter Award in 2017.

YINLIANG DIAO (Member, IEEE) received the B.E. degree from Chongqing University, Chongqing, China, in 2008, the M.S. degree in electronic engineering from the Beijing University of Posts and Telecommunications, Beijing, China, in 2011, and the Ph.D. degree in electronic engineering from the City University of Hong Kong, in 2016. Since 2017, he has been an Assistant Professor with South China Agricultural University, Guangzhou, China. In 2019, he joined the Department of Electrical and Mechanical Engineering, Nagoya Institute of Technology, where he is currently a Research Associate Professor. His current research interests include electromagnetic dosimetry modeling and electromagnetic compatibility. He is a member of IEEE ICES Standards Coordinating Committee, and a member of the Scientific Expert Group of International Commission on Non-Ionizing Radiation Protection. He was a recipient of the Young Scientist Award from URSI GASS 2020.

KENSUKE SASAKI (Member, IEEE) received the B.E., M.E., and Ph.D. degrees in electrical and electronic engineering from Tokyo Metropolitan University, Tokyo, Japan, in 2006, 2008, and 2011, respectively.

He is currently with the National Institute of Information and Communications Technology (NICT), Tokyo. His research interests include electromagnetic theory, bioelectromagnetics, and dielectric properties measurement.

Dr. Sasaki was a member of the Scientific Expert Group of International Commission on Non-Ionizing Radiation Protection (ICNIRP), from 2018 to 2020. He has been the Early Carrier Representative of Commission K, the International Scientific Radio Union (URSI), since 2017. He was a recipient of the 2009 Young Scientist Award of the URSI, the 2012 Best Paper Award of the IEEJ, and the 2020 Achievement Award of the IEICE.

ALEXANDER PROKOP (Member, IEEE) received the M.S. degree in electrical engineering and the Ph.D. degree in computational electromagnetics from Technische Universität Darmstadt, Darmstadt, Germany, in 1997 and 2004, respectively.

He joined the Research and Development Department of CST, in 1998. He is currently the Bioelectromagnetics Applications Director of SIMULIA Research and Development, Dassault Systèmes. Since 2006, he participates in the development of several IEEE/IEC standards on simulation methods and human exposure assessment. He is also a Convenor of IEC TC 106 and IEEE ICES TC34 subcommittees and working groups on computational SAR assessment JMT 62704-3 for mobile phones and JMT 62704-4 using the finite element method. In IEEE APS/SC, he leads a working group within P2816 on simulation of antennas using the TLM method. His research interests include anatomical human body modeling and computational biomedical simulation workflows.

DRAGAN POLJAK (Senior Member, IEEE) received the Ph.D. degree in electrical engineering from the University of Split, Croatia, in 1996. He is currently a Full Professor with the Department of Electron and Computing, University of Split. He has published more than 160 journal articles and 250 conference papers, and authored some books, e.g. two by Wiley, New Jersey, and one by Elsevier, St. Louis. His research interests include computational electromagnetics (electromagnetic compatibility, bioelectromagnetics and plasma physics). He is a member of Editorial Board of Engineering Analysis with Boundary Elements, Mathematical Problems in Engineering, and IET Science, Measurement & Technology. He was awarded by several prizes for his achievements, such as the National Prize for Science (2004), Croatian Section of IEEE Annual Award (2016), Technical Achievement Award of the IEEE EMC Society (2019), and George Green Medal from University of Mississippi (2021). From May 2013 to June 2021, he was a member of the Board of the Croatian Science Foundation. He is also involved in ITER Physics EUROfusion collaboration and in Croatian Center for Excellence in Research for Technology Sciences. He is active in few Working Groups of IEEE/International Committee on Electromagnetic Safety (ICES) Technical Committee 95 SC6 EMF Dosimetry Modeling.

VICKO DORIC (Member, IEEE) was born in Split, Croatia, in April 1974. He received the Ph.D. degree from the University of Split, Split, in 2009.

He is currently an Assistant Professor with the Department of Electronics and Computing, Faculty of Electrical Engineering, Mechanical Engineering and Naval Architecture (FESB), University of Split. To date, he has published two books, 18 journal articles, and 73 conference papers in the area of computational electromagnetics and electromagnetic compatibility. His research interests include computational methods in electromagnetics, particularly in the numerical modeling of wire antenna structures with strong applications in the field of electromagnetic compatibility.

Dr. Doric served as the President of Croatian Chapter of IEEE EMC Society, from 2016 to 2019.

JINGTIAN XI (Member, IEEE) received the B.E. and M.E. degrees in electronic and information engineering from the South China University of Technology, Guangzhou, China, in 2003 and 2006, respectively, and the Ph.D. degree in microelectronics and solid-state electronics from Fudan University, Shanghai, China, in 2009. From 2009 to 2017, he was a Senior Researcher with the Logistics and Supply Chain MultiTech Research and Development Centre (LSCM) founded by the Government of the Hong Kong Special Administrative Region and affiliated to Hong Kong University. Since 2017, he has been a Project Leader at the Foundation for Research on Information Technologies in Society (IT'IS), Zürich, Switzerland. He has authored or coauthored more than 30 publications in journals and conferences, and holds five patents. His current research interests include antenna design, RF dosimetry, and verification and validation (V&V) of numerical/measurement solutions for assessing exposure from electromagnetic sources. He has served as a technical program committee (TPC) member for multiple conferences and a reviewer for various IEEE journals.

SACHIKO KODERA (Member, IEEE) received the B.E. and M.E. degrees in electrical and computer engineering and the Ph.D. degree in computer science from the Nagoya Institute of Technology, Nagoya, Japan, in 2002, 2006, and 2019, respectively.

In 2016, she joined the Department of Electrical and Mechanical Engineering, Nagoya Institute of Technology, as a Researcher. She is currently a Research Assistant Professor. Her current research interests include electromagnetic and thermal dosimetry modeling in humans for radio-frequency and ambient heat exposures. She is a member of IEICE. She received several awards, including Prizes for Science and Technology (Public Understanding Promotion Category in 2020) from the Commendation for Science and Technology, Minister of Education, Culture, Sports, Science, and Technology, Japan.

AKIMASA HIRATA (Fellow, IEEE) received the B.E., M.E., and Ph.D. degrees in communications engineering from Osaka University, Suita, Japan, in 1996, 1998, and 2000, respectively.

From 1999 to 2001, he was a Research Fellow of the Japan Society for the Promotion of Science, and also a Visiting Research Scientist at the University of Victoria, Victoria, BC, Canada, in 2000. In 2001, he joined the Department of Communications Engineering, Osaka University, as an Assistant Professor. In 2004, he joined the Department of Computer Science and Engineering, Nagoya Institute of Technology, as an Associate Professor, where he is currently a Full Professor. His research interests include electromagnetic safety, risk management system for heat-related illness, methods in neuroscience, antennas, filters, and related computational techniques.

Prof. Hirata is a fellow of Institute of Physics, and a member of IEICE, IEE Japan, and Bioelectromagnetics Society. He is an Editorial Board Member of *Physics in Medicine and Biology*, a member of the Main Commission and a Chair of Project Group of International Commission on Non-Ionizing Radiation Protection, and a member of Administrative Committee and a Subcommittee (EMF Dosimetry Modeling) Chair of IEEE International Committee on Electromagnetic Safety, and an Expert of World Health Organization. From 2006 to 2012, he was also an Associate Editor of the IEEE TRANSACTIONS ON BIOMEDICAL ENGINEERING. He received several awards, including Young Scientists' Prize (2006) and Prizes for Science and Technology (Research Category 2011, Public Understanding Promotion Category 2014, 2020) by the Commendation for Science and Technology by the Minister of Education, Culture, Sports, Science, and Technology, Japan, and IEEE EMC-S Technical Achievement Award (2015), and the Japan Academy Medal and JSPS Prize (2018).

WALID EL HAJJ (Member, IEEE) received the National Degree of Master for his Research in ''microwave materials and devices for communication systems'' and the Ph.D. degree in information and communications sciences and technologies from Telecom Bretagne, Brest, France, in 2008 and 2011, respectively.

From 2011 to 2013, he was a Researcher with the LabSTICC/MOM Laboratory, Microwave Department, Telecom Bretagne. He joined Intel Corporation, in 2014. He is currently a Scientist Officer at Intel Wireless RF Laboratory (ISO 17025 Certification Laboratory), Wireless Test and Certification Center Group. He is leading the different research and development activities related to new wireless technologies and products certification. He is participating and leading several standardization efforts in the human exposure and product safety domain. He is mandated as expert in French Standardization Association (AFNOR). Since 2017, he participates in the development of several IEEE/IEC standards on human exposure computational and measurement assessments.

Dr. El Hajj is a member of IEC TC 106 and IEEE ICES TC95. He is also a member of CMC TF Radio Group, IECEE. He is the Convener of Working Group 5 under Subcommittee 6 of IEEE ICES TC95 established to study the different aspects of incident power density definition in correlation with temperature elevation.